JOURNAL OF PROPULSION AND POWER
Vol. 15, No. 2, March–April 1999

Three-Dimensional Flowfield Downstream of an Axial-Flow Turbine Rotor

D. Ristic,* B. Lakshminarayana,† and S. Chu‡
Pennsylvania State University, University Park, Pennsylvania 16802-1400

A systematic and comprehensive investigation was performed to provide detailed data on the three-dimensional viscous flow phenomena downstream of a modern turbine rotor and to understand the flow physics such as the origin, nature, development of wakes, secondary flow, and leakage flow. The experiment was carried out in the Axial Flow Turbine Research Facility at Pennsylvania State University, with velocity measurements taken with a three-dimensional laser Doppler velocimetry system. Two radial traverses at 1 and 10% of chord downstream of the rotor were performed. Sufficient spatial resolution was maintained to resolve blade wake, secondary flow, and tip leakage flow. The wake deficit is found to be substantial, particularly at 1% of chord downstream of the rotor. At this location, negative axial velocity occurs near the tip, suggesting flow separation in the tip clearance region. Cross correlations are mainly associated with the velocity gradient of the wake deficit. Radial velocities, in the wake and the endwall region, are found to be substantial. Two counter-rotating secondary flows are identified in the blade passage, with one occupying the half-span close to the casing and the other occupying the half-span close to the hub. The tip leakage flow is restricted to 10% immersion from the blade tip. There are strong vorticity distributions associated with these secondary flows and tip leakage flow. The passage-averaged data are in good agreement with design values.

Nomenclature

c_r	= rotor blade axial chord at midspan
H	= normalized distance between the hub and the casing, $(r - r_h)/(r_t - r_h)$
L	= semiwake width
$\dot{m}$	= mass flow rate
N	= number of measurements per bin
r_h, r_t	= hub and tip radius
S	= tangential distance normalized by blade spacing
s, n, r	= streamwise, normal, and tangential directions
U_m	= blade speed at midspan
V	= absolute velocity
v'	= fluctuating velocity components (normalized by local velocity)
W	= relative velocity
W_c	= relative velocity defect at the wake centerline
w'	= fluctuating relative velocity
$\overline{w_i' w_j'}$	= shear stress
x, r, θ	= axial, radial, and tangential direction, $x/c_r = 0$ at leading edge, = 1 at trailing edge
Z	= normalized axial distance, x/c_r
α	= absolute flow angle
β	= relative flow angle measured from the axial direction
β_0	= relative flow angle at trailing edge
γ_1, γ_2	= laser Doppler velocimetry channel angles
Ω	= rotor angular velocity
ω_x	= axial vorticity, Eq. (3)

Subscripts

BA, BP	= blade aperiodic and periodic components
e	= ensemble average
RP, RA	= revolution periodic and aperiodic
s, n, r	= streamwise, normal, and radial directions
x, r, θ	= axial, radial, and radial direction
1, 2, 3	= upstream of nozzle, upstream of rotor, downstream of rotor positions

Introduction

THE flowfield in an axial-flow turbine rotor is three dimensional. The three-dimensional viscous effects include blade and endwall surface (laminar, transitional, and turbulent) boundary layers, shock-boundary-layer interaction, blade wake, horseshoe vortex near the blade leading edge, tip leakage flow, and the secondary flow. Much of the research work on turbine rotor flows has been confined to measurements in cascades, and substantial understanding of the three-dimensional flowfield in the blade passage has been gained. The pioneering work by Langston et al.[1] of secondary flow patterns in a turbine cascade gave a detailed description of the passage vortex and the leading-edge horseshoe vortex. Sieverding[2] summarized extensive results of experimental investigations on the evolution of horseshoe and passage vortices and on the effect of vortex structures on endwall boundary layers. Gregory-Smith et al.[3] acquired valuable data in the secondary flow region in a cascade, including turbulent stresses, intensities, and losses. The tip leakage flow was the subject of many turbine cascade researches, and a recent work by Yamamoto[4] in a cascade demonstrated the strong effect of gap size and inlet incidence on the leakage flow and the passage vortex.

Because of the general industry trend toward highly three-dimensional blading geometry to meet the requirement of increased aerodynamic efficiency with fewer turbomachine components, investigations related to flow conditions in real turbine stages have been intensified. Joslyn and Dring[5] measured the mean properties of the three-dimensional flowfield in a single-stage turbine using the five-hole probe (FHP) area traversing in the rotating frame. Gallus et al.'s[6] experimental and numerical results demonstrated a much improved predic-

Received Aug. 1, 1997; revision received July 23, 1998; accepted for publication Aug. 11, 1998.

*Graduate Student, Center for Gas Turbines and Power, Department of Aerospace Engineering.

†Evan Pugh Professor of Aerospace Engineering and Director, Center for Gas Turbines and Power, Department of Aerospace Engineering, 153 Hammond Building. Fellow AIAA.

‡Postdoctoral Visiting Research Assistant, Center for Gas Turbines and Power, Department of Aerospace Engineering.

tion of the rotor passage vortex and the flow exit angle near the hub by considering the unsteady interaction between the stator secondary flow and the rotor flowfield. They also found that the tip leakage vortex is confined to a region very close to the shroud because of a very tight tip clearance.

The objective of this study was to investigate the three-dimensional viscous flow phenomena downstream of a modern turbine rotor blade passage and to understand the flow physics such as origin, nature, and interaction, and their effect on the overall performance. The velocity measurements were carried out in the turbine facility with a three-dimensional laser Doppler velocimeter (LDV).

Facility and Instrumentation

The Axial Flow Turbine Research Facility (AFTRF) at Pennsylvania State University is an open-circuit, single-stage facility with a diameter of 91.4 cm and a hub-to-tip ratio of 0.73, with 23 nozzle guide vanes and 29 rotor blades. The configurations of the vane and blade are designed by General Electric Aircraft designers and represent the features of a current or near-future high-pressure turbine stage. Details of blading, design, velocity triangles, and facility instrumentation are given by Lakshminarayana et al.[7] The peak total-to-total isentropic efficiency is 89.3% at a rotational speed of 1300 rpm. At this peak efficiency point, the total pressure and temperature ratios are P_{03}/P_{01} = 0.928 and T_{03}/T_{01} = 0.981, respectively. The experiment was conducted at a corrected rotational speed of 1300 rpm and a mass flow rate ($\dot{m}$) of 10.53 kg/s. Design features of the AFTRF are shown as follows. Hub tip ratio = 0.7269; tip radius = 0.4582 m; blade height = 0.1229 m; tip relative Mach number = 0.240 (maximum); rotor blade (tip): number = 29; chord = 0.1287 m; spacing = 0.1028 m; turning angle = 95.42 deg (tip), 125.69 deg (hub); maximum thickness = 22 mm; tip clearance = 0.97 mm average; nozzle guide vane (tip): number = 23; chord = 0.1768 m; spacing = 0.1308 m; turning angle = 70 deg; maximum thickness = 38.81 mm; vane Reynolds number: based on inlet velocity (3–4) × 10^5; based on exit velocity (9–10) × 10^5; and Blade Reynolds number: based on inlet relative velocity (2.5–4.5) × 10^5; based on exit relative velocity (5–7) × 10^5.

The flowfield inside the nozzle and at the exit of the nozzle has been acquired with a FHP and a hot-wire (HW) probe, and some of these data are reported by Zaccaria and Lakshminarayana.[8] The earlier measurement locations are shown in Fig. 1a. The measured velocity profiles and angles at inlet to the rotor (about 10% chord upstream of the rotor) is shown in Fig. 2. The total turbulence intensity was 7% near midspan. The secondary flow near the casing and the hub introduces flow overturning of the absolute flowfield. The boundary layers are highly skewed near the hub and the tip, and the boundary-layer thickness (based on axial velocity) is about 10% span near the hub and 20% span near the casing. The absolute total velocity is nearly constant through the boundary layer. Hence, the flow enters the rotor with the normal and the streamwise components of vorticity.

The LDV system is a three-color cross-beam system (TSI model 9100-12). The light source is a 7-W argon–ion laser (Coherent model Innova.300), operating in the multiline mode. As shown in Fig. 1, the blue and green light beams are introduced into the flowfield, in one optical rail, perpendicular to the glass window on the turbine casing to sample axial and tangential components of the velocity. The violet beam is arranged in another optical rail with an angle 27.8 deg from the perpendicular to measure the radial component. In addition, 32.5- and 45-deg angle arrangements are also tried in the measurements, and it is found that the configuration with about a 30-deg angle gives a sufficient resolution of the radial velocity while still keeping the system manageable. Frequency shifting of 40 MHz is used to reduce the fringe bias and to solve the direction ambiguity by passing one of the two crossing beams through a Bragg cell. Liquid particles with a nominal mean particle size of about 0.6 μm, generated by a six-jet atomizer

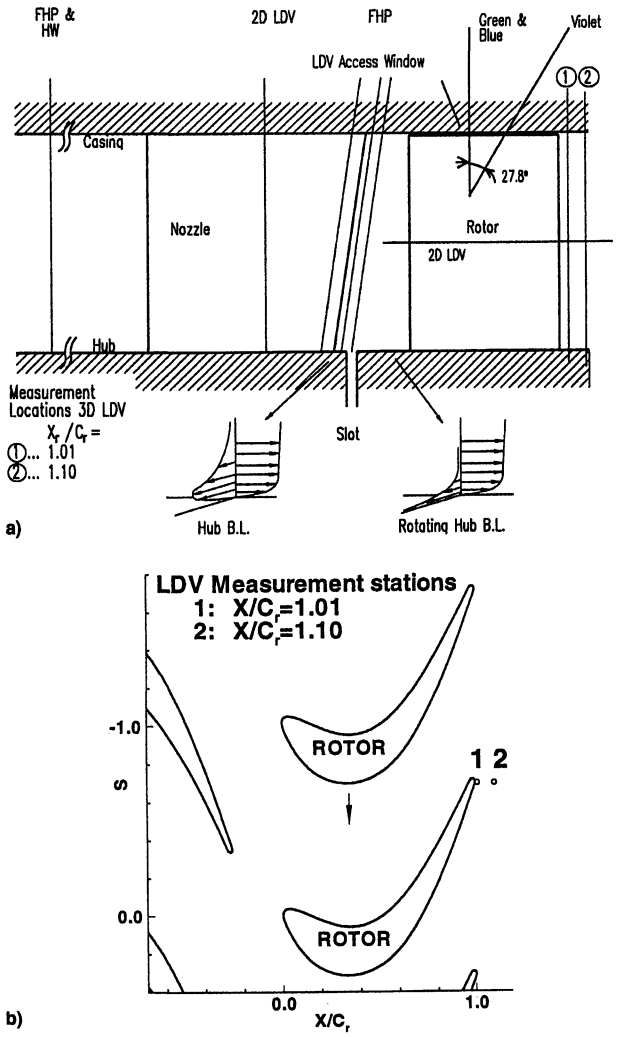

Fig. 1 a) Schematic of the test section with locations of previous and current measurement locations and b) axial and tangential location (with reference to nozzle of LDV measurement).

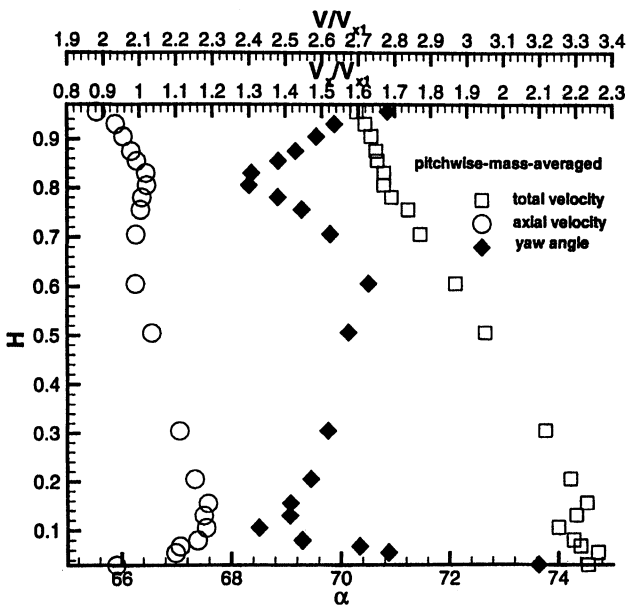

Fig. 2 Measured absolute flow angle and velocity at the inlet of the rotor.

(TSI model 9306), are introduced into the flowfield at the bellmouth inlet of the facility as the seeding particles. In selecting the working liquid for the atomizer, propylene glycol is decided on largely as a result of its low toxicity and water solubility. The latter is especially helpful for the investigations of the tip leakage flow because the seeding particles directly contaminate the glass window and the water solubility allows for a quick clean-up during the experiments.

A personal computer-based interface (Dostek model 1400A) records the three velocity component data along with the rotor orientation from a shaft encoder (6000 pulses per revolution clocking and 1 pulse per revolution triggering). All measurements were acquired with the facility operating at peak efficiency.

The data reduction is accomplished by ensemble averaging and then by passage-to-passage averaging according to the recorded rotor orientation. The entire rotor is discretized into 1450 bins (windows) (50 per blade passage) and the corresponding measurements are averaged over the individual bins to yield the ensemble-average velocity. One of the main limitations of the LDV technique is apparent in the nonuniform distribution of measurements across the individual blade passages shown in Fig. 3. A fairly low seed density in the secondary flow region required an increased run time to acquire sufficient measurements to resolve the blade-to-blade variations accurately. To determine the minimum number of data points per bins required for a sufficient passage averaging, the mean velocity and turbulence intensity (the rms value of the instantaneous velocity minus the passage-averaged mean) were examined at various stations with sample sizes from 30,000 to 200,000. The passage-averaged properties were computed and compared for a variety of individual bin measurements and found to be essentially constant for samples larger than 100 measurements per bin.

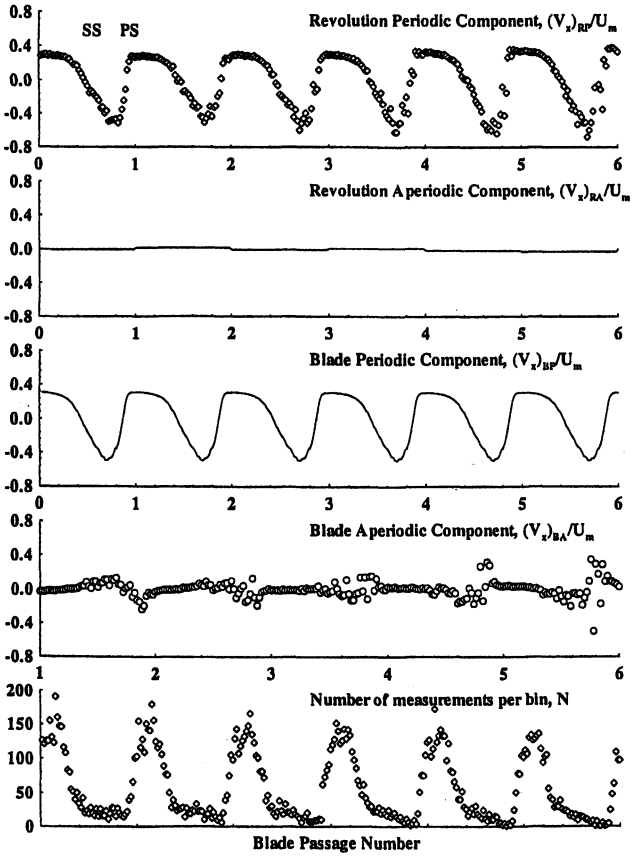

Fig. 3 Blade periodic, blade aperiodic, revolution periodic, and revolution aperiodic components at x/c_r = 1.01 (1% chord from trailing edge) and H = 0.93 position.

In addition, the actual number of data bins per blade passage, each representing a finite time interval, was varied to determine the optimal size. If within this time interval there exists appreciable variation in velocity, particularly in the wake region, artificial fluctuations may influence the averaging procedure and result. The number of bins per blade passage was varied between 50 and 100 at a few selected stations with large-velocity gradients, and negligible variations were seen between the two temporal discretizations. A sample size of 50 was chosen to keep the overall data sample size manageable, while ensuring measurement accuracy.

The following data are derived, presented, and interpreted in this paper: 1) three components of mean velocity in the cylindrical coordinate system (r, θ, and z); 2) secondary velocity vectors and axial vorticity; and 3) total turbulence intensity and stresses in the intrinsic coordinate system (s, n, and r).

The intrinsic coordinate system (s, n, and r) is also used to derive the mean velocities, turbulence intensities, and stresses. This provides valuable information on the stresses in the streamwise and radial directions. In this coordinate system, s is the streamwise direction, n is the principal normal (blade-to-blade) direction, and r is the radial direction. The s coordinate is aligned with the design exit flow angle. Any deviation from this angle is the secondary flow represented by

$$\boldsymbol{W}_{\text{spc}} = \boldsymbol{W}_{\text{measured}} - \boldsymbol{W}_{\text{design}} \tag{1}$$

The mean velocities presented in this paper are based on the averaged passage derived from averaging the ensemble-averaged velocity across all of the blade passages. This procedure is considered valid for the investigation of single-stage flowfield of the AFTRF. To verify that the averaging procedure is valid, the procedure developed by Suder et al.,[9] and later modified by Suryavamshi et al.,[10] to decompose the instantaneous velocity measurement in a multistage environment was used at a few selected measurement stations. The decomposition is based on

$$V = \bar{V} + V_{\text{BP}} + V_{\text{BA}} + V_{\text{RA}} + v' \tag{2}$$

where $\bar{V}$ is the time mean, V_{BP} is the blade periodic, V_{BA} is blade aperiodic, V_{RA} is the revolution aperiodic, and v' is the unresolved unsteadiness caused by turbulence and revolution-to-revolution variations. The summation of V_{BP} and V_{BA} represents the revolution periodic (V_{RP}) component. The general procedure in the computation of the individual components involves computation of $\bar{V}$ and the ensemble average (V_e) over the entire turbine rotor. The V_{RA} component is computed as the average variation of the difference between the time mean and ensemble-averaged velocity over the individual blade passage. For a single-stage facility, the V_{RA} component is essentially zero. The revolution periodic (V_{RP}) component is computed by subtracting the V_{RA} component from $V_e - \bar{V}$ at each bin location. The V_{RP} component can now be decomposed into V_{BP} and V_{BA} components. The blade periodic is representative of the flow as seen by the average blade passage, and the blade aperiodic component is a measure of the blade-to-blade passage variation. Figure 3 shows the relative magnitudes for the axial velocity components in the first six blade passages at x/c_r = 1.01 and H = 0.93 locations. As expected, the V_{RA} velocity component is negligible (maximum of $0.02U_m$). The blade aperiodic component is relatively small over most of the blade passage, except in the wake region.

To assess the fluctuation in velocity caused by the variation between individual blades involved in the passage-averaging process used in this study, a large amount of data is sampled at one location (x/c_r = 1.10 and 95% span), with at least 1500 data points per window. Thus, the minimum data number per window for each individual blade passage is about $1500/29 \approx 51$. As a demonstration of this argument, the axial turbulence

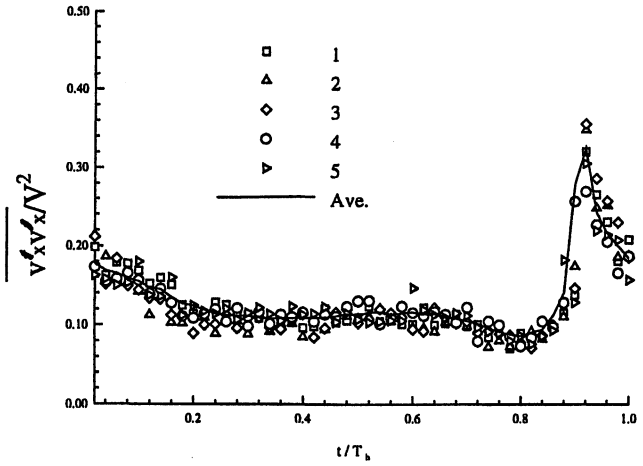

Fig. 4 Axial turbulence intensity distributions for five individual blade passages (based on ensemble-averaged velocity) and for the averaged blade passage.

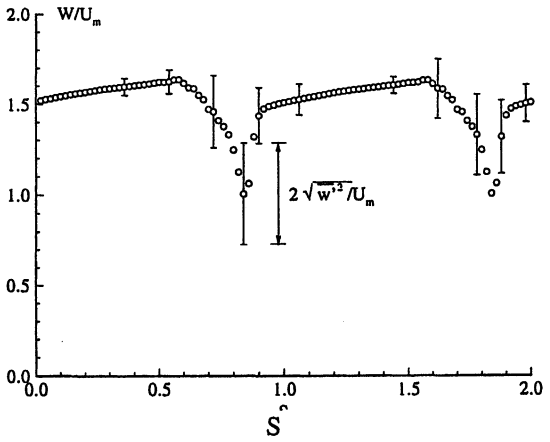

Fig. 5 Total relative velocity 1% downstream of the rotor at H = 0.6. The vertical bars indicate the total unresolved unsteadiness at the measurement location.

intensity for five individual blade passages (based on the ensemble-averaged mean) and for the average passage are plotted in Fig. 4. The clustering of individual blade passage data around the average passage suggests that the turbulence intensity distribution is nearly identical in all passages.

This clearly demonstrates that the passage-averaging procedure can be used to derive the blade-to-blade variation of the three components of velocity. The passage-average properties are then used to derive the unresolved unsteadiness in the rotor passage using Eq. (2). The unresolved unsteadiness at x/c_r = 1.10 and H = 0.6 is shown superposed on the blade periodic quantities in Fig. 5.

Two radial traverses of LDV measurements (a total of 18 radial locations with higher resolution near the blade tip) were completed at 1 and 10% chord lengths downstream of the rotor trailing edge (denoted as x/c_r = 1.01 and = 1.10 and shown in Fig. 1b) to identify the various flow features. Some of the data are presented and discussed next. For a complete data set, see Ristic et al.[11]

Blade-to-Blade Profiles

The mean axial, radial, and relative tangential velocity; turbulence intensity; and shear-stress profiles are shown in Fig. 6 for a few selected radial locations at the x/c_r = 1.01 station.

The mean velocity profiles at x/c_r = 1.01, shown in Fig. 6, clearly indicate the presence of a thick boundary and wake on the suction side and a thin boundary layer and wake on the pressure side. The fact that the suction surface boundary layer wake is substantially thicker than that on the pressure side indicates that the probable cause of this is the transport of nozzle wake toward the suction side (unlike the compressor). This results in a higher-velocity defect and higher-turbulence intensities. Near the casing (H = 0.93 and 0.98), the flow is nearly fully developed, with substantial radial inward velocity near the suction surface caused by the secondary flow. Very strong secondary flows and leakage flows interact in this region. The flow in the secondary flow regions is overturned and the turbulence intensities are high. The near-wake features, where the turbulence intensities are lowest in the wake center, can also be clearly seen. Furthermore, the radial component of turbulence intensities are higher than the streamwise component in the wake and secondary flow regions, thus confirming the effect of rotation in modifying the turbulence structure. The Coriolis forces tend to increase the turbulence intensities in the radial direction inside the rotor boundary layer, and this is consistent with the turbulence measurement and analysis inside an inducer rotor,[12] and at the exit of a compressor rotor.[13] The shear stresses in the streamwise direction ($\overline{w_s' w_n'}$) are higher than those in the radial direction.

The data away from the casing (H = 0.5 in Fig. 6) shows that the suction surface boundary/wake thickness decreases toward midspan, being fairly thin with low radial velocities at the midradius. One of the interesting features observed at H = 0.8 is the presence of thick wakes and high-turbulence intensities. The probable cause of this is the presence of nozzle secondary flow that was observed at this location.[8] The data in the hub region (at H = 0.1 in Fig. 6) indicate the presence of a very large radial outward velocity, with a thick wake on the suction side corner. The wake description is incomplete as a result of inaccessibility in this region by the LDV.

The freestream turbulence intensities vary from 3 to 5% across the span, with the exception of locations very close to the hubwall region. The turbulence intensity at inlet to nozzle vanes varies from 1 to 1.5%. Hence, the freestream turbulence has increased as a result of the interaction of the nozzle wake with the rotor flowfield.

The region from 20 to 60% span (Fig. 6) is found to be dominated by an inviscid core (where the flow is uniform) and the blade wake. The thinnest wake occurs at H = 0.5 and the wake becomes increasingly wider toward the endwall regions. No core or inviscid flow region is found near the casing or hubwall regions.

Secondary and Leakage Flowfield

The secondary velocity vectors, defined by Eq. (1), are shown in Fig. 7. Five distinct regions of the flowfield can be identified: passage core flow, hub passage vortex, casing passage vortex, rotor wake flow, and the tip vortex flow. The blank region near the hub blade region at x/c_r = 1.01 is caused by inaccessibility of the flowfield by the laser. It is clear that there are two secondary flow regions in the blade passage. Toward the hub, a strong, well-organized secondary flow pattern occupying the entire half-span is observed, caused by a large blade turning angle. Its center is at ~20% pitch from the blade suction side and between H = 0.30 and 0.20 immersion. However, the secondary flow and leakage flow in the casing half of the passage are much more complicated and stronger. The radially outward flow on the blade pressure side possesses significant radial outward velocity only when it is very close to the casing (within 15% of the blade passage). The radially inward flow on the blade suction side, nevertheless, covers the whole half-span and is induced by the secondary flow. The core of the secondary vortex is located near H = 0.85 and S = 0.4. The secondary flow tends to hug the tip leakage vortex and contains it in the suction surface-casing corner. The leakage flow phenomena observed here is substantially different from those observed in cascades.[4] Unlike cascades, the tip clearance vortex is confined to a small region near the suction surface-casing corner. The relative motion between the sta-

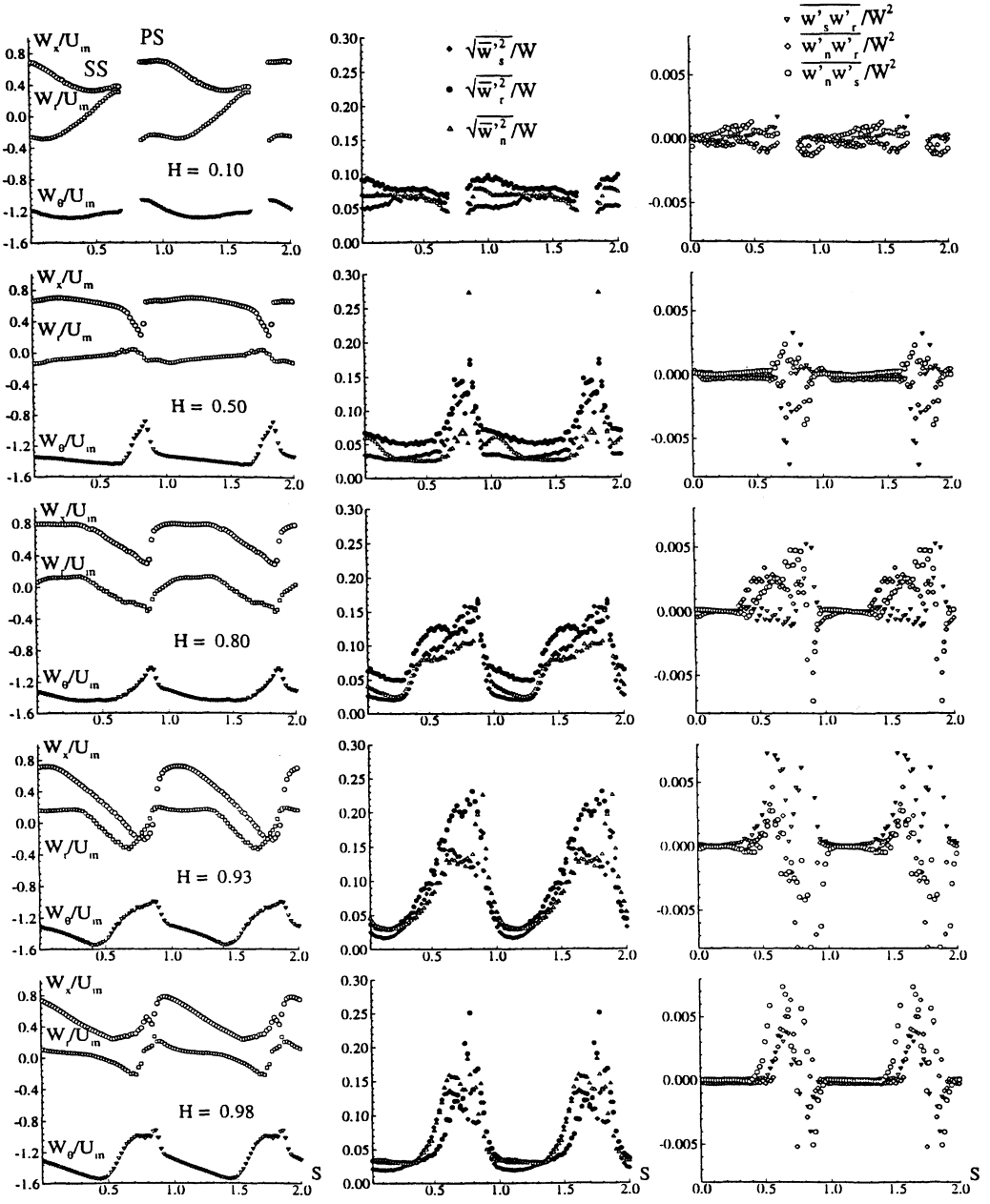

Fig. 6 Blade to blade velocity and turbulence distributions at x/c_r = 1.01. The streamwise direction is based on design exit angles.

tionary wall and the moving blade tends to confine the leakage vortex to the suction side of the blade. In addition, the rotation effects prevent radial inward transport of the secondary flow core. These are the major features not simulated in the cascade test. In cascades, the leakage flow has a tendency to move much farther away from the casing and suction surface. The secondary flow and vortex has a much stronger influence than the leakage vortex for this particular rotor.

Because of the leakage flow, the secondary flow pattern in the casing-half of the passage becomes very distorted. The leakage and secondary vortices entrain fluid from surroundings as confirmed by the outward velocity near the pressure side and inward velocity on the suction side. The secondary flow is confined to the region above H = 0.90. Below H = 0.90, high radial velocity (inward) occurs in the wake–secondary flow interaction region. This region has radial inward velocity and involves the interaction and mixing of the rotor wake and secondary flow. It is characterized by the radial flows, low total velocity, and high vorticity, as will be explained later in this paper. Thus, it is clear that rotor wakes are influenced substantially by the secondary flow from midradius to tip, with secondary flow effects dominating (over rotation effects) in inducing inward flows.

Farther downstream at x/c_r = 1.10 (Fig. 7b), the leakage flow weakens. The secondary flow becomes dominant near the blade suction side-casing corner. The zero radial flow velocity region on the blade suction side moves inward up to H = 0.85. The remainder of the flow features remains the same as x/c_r = 1.01, but at a slightly weaker level. One of the interesting features of this flowfield is that the growth and diffusion of leakage vortex are substantially less than those observed in cascades. The vortex tends to stay near the suction surface corner closer to the casing, and its extent is reduced. This is brought about by strong secondary flows, which counteract and prevent growth and spreading of the leakage vortex. The wake region from the hub to midspan region has a radial outward velocity; this is consistent with the effects of rotation on blade boundary layer and wake. The rotation and secondary flow effects have a cumulative effect in inducing large radial outward flow in the wake regions from the hub to midradius.

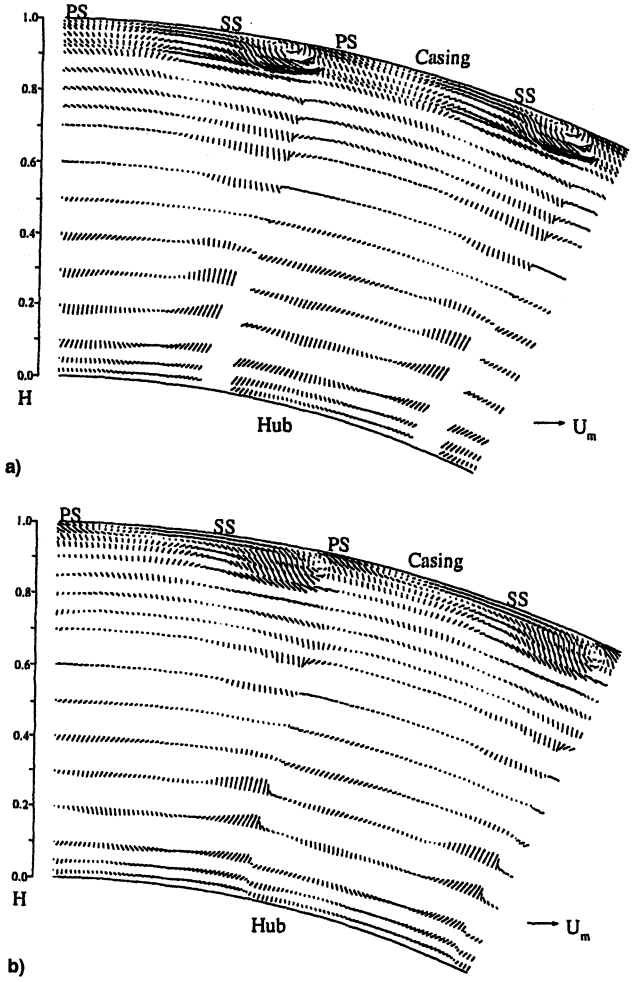

Fig. 7 V_{sec} at a) 1% (x/c_r = 1.01) and b) 10% (x/c_r = 1.10) of chord downstream of the rotor.

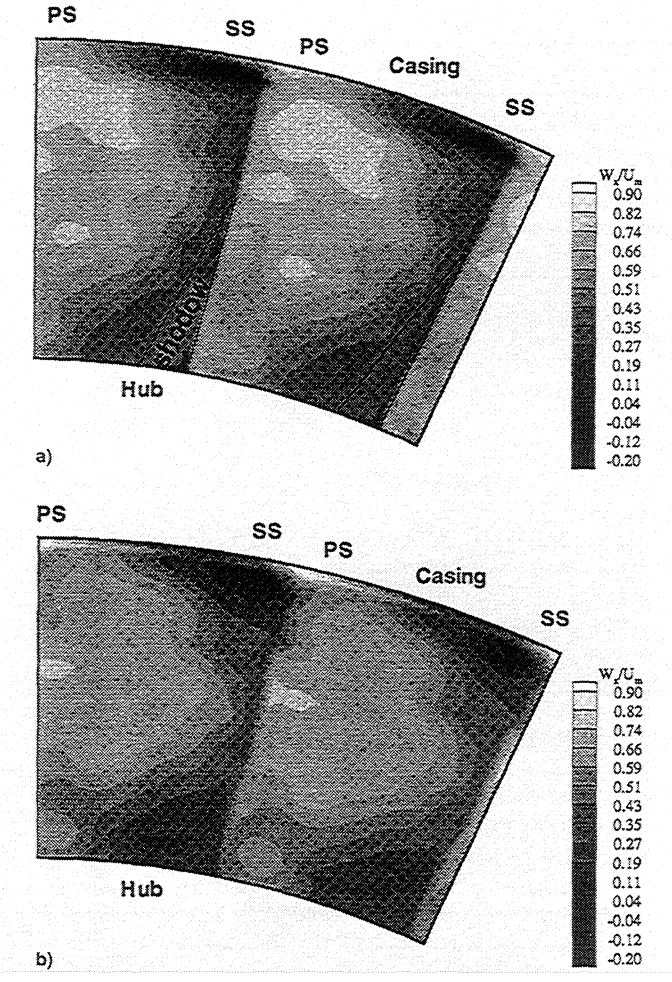

Fig. 8 Axial velocity W_x/U_m contours downstream of the rotor. x/c_r = a) 1.01 and b) 1.10.

Contours of Mean Velocity Components

The contour plots of axial, relative tangential velocity, and relative flow angles at x/c_r = 1.01 and 1.10 are plotted in Figs. 8, 9, and 10, respectively. In the midspan region, the wakes are thin and axial velocities are high. The secondary and leakage flow regions have complex flow characteristics. The wake width increases continuously from midspan to hub and midspan to casing; the endwall region ($H < 0.1$, $H > 0.9$) shows a nearly fully developed flow. The tip clearance region has a separated flow, with substantial negative axial velocities. The secondary flow region (around $H = 0.85$) shows reduced axial velocities. The blockage effects caused by secondary and leakage vortices/flows are also evident from this plot. The region away from these flows shows very high axial velocities extending all the way from $H = 0.6$ to 0.9. As the flow progresses downstream from x/c_r = 1.01 to 1.1, the reversed flow disappears, the wake defect decreases, and the blockage effect caused by secondary and leakage vortices decreases near the casing regions. This is evident from increased axial velocities in regions away from the blade near the casing. For these changes, the distribution is similar to that observed at x/c_r = 1.01.

The relative tangential velocity (W_θ) is shown in Fig. 9. The tip vortex has low axial and relative tangential velocities. In the adjoining secondary flow region, the relative tangential velocity increases rapidly away from the blade, indicating the usual overturning caused by secondary flow and vortex. The core of this vortex is located near $H = 0.85$ closer to the suction side. Below this core, the relative tangential velocity decreases, indicating flow underturning in this region. This confirms the earlier conclusion that the secondary flow dominates the outer span of the rotor.

The measured values of flow outlet angles are shown in Fig. 10. As demonstrated in the contour map, in the core inviscid flow region, the measured flow angle is very close to the design value. In the wake region, a distinctive pattern exists. On the blade suction side, the flow is overturned, and on the pressure side, the flow is underturned. Near the midradius, the relative flow angle changes from −79 deg on the suction side to −56 deg on the pressure side. Near the hub, particularly near the blade suction side-hub corner, the flow is overturned as a result of strong secondary flow toward the blade suction side (x/c_r = 1.01; see Figs. 7 and 10). The flow overturning caused by the casing secondary flow at the blade suction side-casing corner is also visible, but it is overpowered by the tip leakage flow. The leakage vortex and associated very low axial velocity results in the flow angle approaching −90 deg. In fact, at x/c_r = 1.01, negative axial velocity exists in the tip leakage vortex and the flow angle is beyond −90 deg. The influence of tip leakage and secondary flows on the flow angle is so strong and extensive that the previously described wake pattern of the flow angle distribution (overturning on the blade suction side, underturning on the pressure side) is completely distorted for $H > 0.7$ (see Fig. 10; x/c_r = 1.01). On the blade pressure side, the tip leakage flow causes flow underturning in a very confined region near the tip gap.

Near the midspan region ($H = 0.4$–0.85), the axial and radial velocity variation (Fig. 7) is very small outside the wake region. The W_θ variation across the blade passage is nearly linear, influenced by the blade-to-blade pressure gradient. In the wake, the velocity defect is quite large, accounting for a drop

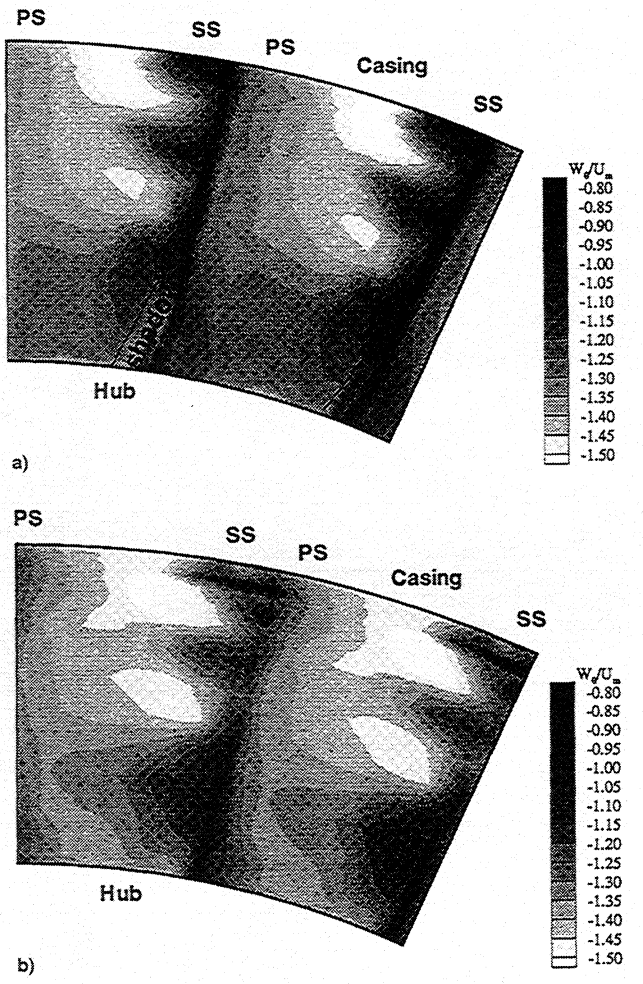

Fig. 9 Relative tangential velocity W_x/U_m contours downstream of the rotor. x/c_r = a) 1.01 and b) 1.10.

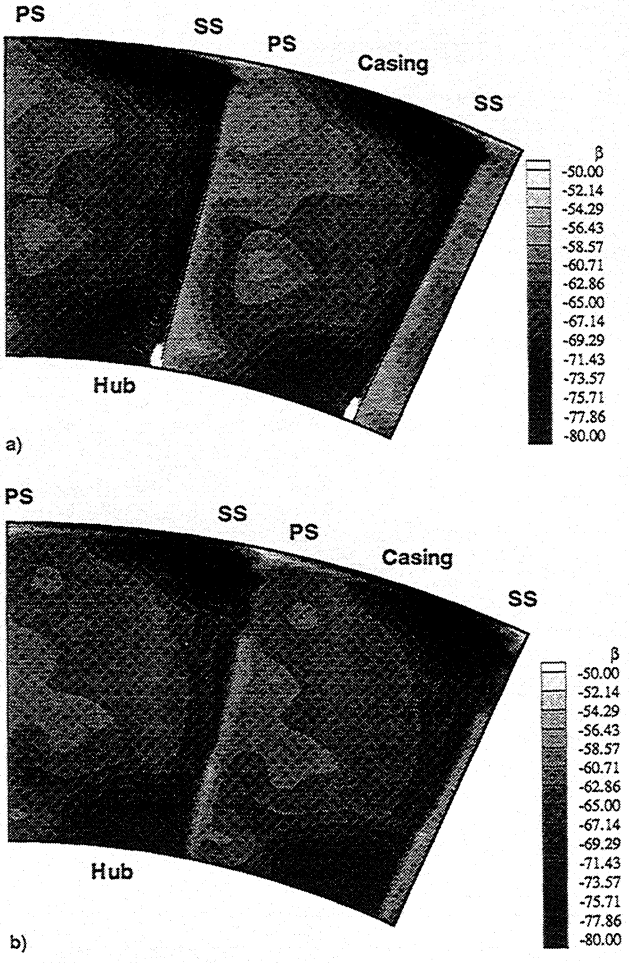

Fig. 10 Relative flow angle β downstream of the rotor. x/c_r = a) 1.01 and b) 1.10.

in the axial velocity from a freestream value of $0.7U_m$ to a minimum of only $0.18U_m$ in the wake. Toward the tip region, the wake width increases as a result of the casing suction passage vortex interacting with the low-momentum fluid in the wake region. At the same time, the radial velocity variation grows dramatically from almost negligible levels in the midspan locations to large radially inward levels of $-0.42U_m$ at $H = 0.7$ (Fig. 7). Toward the tip, the radial velocity starts to drop, as the secondary flow influence decays, until near the $H = 0.93$ location.

In the tip clearance region extending from approximately $H = 0.95$ to the casing, the radial and axial velocity profiles start to exhibit very large gradients caused by the complex interaction between the casing endwall boundary layer, tip clearance vortex, and the blade wake. The tip clearance vortex is clearly visible in the radial velocity profiles at $H = 0.95$ and 0.97 (Figs. 7 and 8), with very high-velocity gradients on either side of the vortex. The tangential velocity profiles in this region still exhibit a large linear gradient region in the freestream and a relatively small wake region when compared with the axial and tangential velocity profiles.

The measured velocity and angle distributions at 10% chord downstream exhibited similar behavior to that at the 1% location (Figs 7–10). The major difference is in the suction-casing corner, where the overall level of axial velocity decreased toward zero compared with the negative velocity region at $x/c_r = 1.01$. The decay is a result of mixing and diffusion caused by the radial outward motion of the tip clearance vortex and an increase in the wake width in the downstream direction. The overall flow features remain very similar, indicating a strong and well-established secondary flow pattern propagating downstream. In general, the following conclusions can be drawn with regard to the flow variation in the downstream direction $x/c_r = 1.01-1.10$:

1) The radial velocities are slightly lower at the downstream location as a result of mixing and decay.

2) The hub passage vortex remains well organized and at the same position relative to the blade passage.

3) The casing passage vortex moves toward the suction side of the wake because of the low-pressure region created by the tip clearance vortex and the overall blade-to-blade pressure gradient. There is very little movement of the passage vortex in the radial direction as the flow progresses downstream.

4) The tip-clearance vortex remains well organized, decays in strength, and moves slightly inward radially as a result of the radial pressure gradient and the large-scale casing passage vortex motion.

There are major differences in the secondary and leakage flows observed in cascades and rotors. It is evident that the underturning region is small and confined to a small region near the blade tip and the pressure side of the wake (Fig. 10). Substantial secondary flow, near the hub and tip regions, results in overturning, with the highest values reaching -80 deg (15-deg overturning). It is also evident that the rotor flowfield is appreciably different from those observed in a cascade. The blade motion tends to confine the tip vortex to the corner. In addition, the blade motion also prevents secondary vortex and loss core from moving radially inward and toward the midpassage (Figs. 7–10). The casing secondary flow is confined to the tip region, but the hub secondary flow region, augmented by both rotation and secondary velocities, tends to spread out more.

Axial Vorticity

Only the axial component of vorticity can be derived exactly because all of the velocity gradients can be calculated in (r, θ) directions from the measured data. The gradients in the axial direction are not accurate because of the coarse measurement grid. The axial vorticity is calculated from

$$\frac{\omega_x}{\Omega} = \frac{1}{r}\frac{\partial(rW_\theta)}{\partial r} - \frac{\partial W_r}{r\partial\theta} \tag{3}$$

The contours of axial vorticity are shown in Fig. 11. The negative values indicate anticlockwise motion. The leakage vorticity is confined to the casing within 5% of the span in the blade suction side corner. The wake vorticity is positive (because of inward radial velocity) in the outer span. The secondary vorticity (negative) near the casing region is a dominant feature of the flowfield, as indicated earlier, and it covers substantial portions of the passage. A negative vorticity distribution exists in a more fragmented form as a result of the interaction between the secondary flow, the leakage flow, and the wake. On the suction side and within 15% radial immersion, the vorticity is negative. Similarly, the secondary vorticity is very strong near the hub region and the maximum strength is between the hub and midspan region, closer to the suction surface. The highest level of this vorticity distribution occurs at $H = 0.35$ immersion and 15% pitch from the blade suction side, which is also the region of high-turbulence intensity (as explained later). The strength of the maximum leakage vorticity, secondary vorticity in the hub, and endwall regions are about the same orders of magnitude. One of the major features, not alluded to before, is the wake-secondary flow interaction near the casing. The secondary motion induces radial inward flow near the suction side. The rotation induces radial outward flow in the blade wake. This combined with the secondary transverse motion results in interaction with the blade wake generating additional vorticity. This region covers ~60–80% of the span and is characterized by the negative (anticlockwise) vorticity in this region. Likewise, near the hub ($x/c_r = 1.1$), the interaction between the secondary flow and the wake (augmented by rotation effects) results in positive vorticity, which is clockwise as opposed to the secondary vorticity. These interaction effects were simulated numerically in a cascade and are known to increase mixing losses downstream.[14]

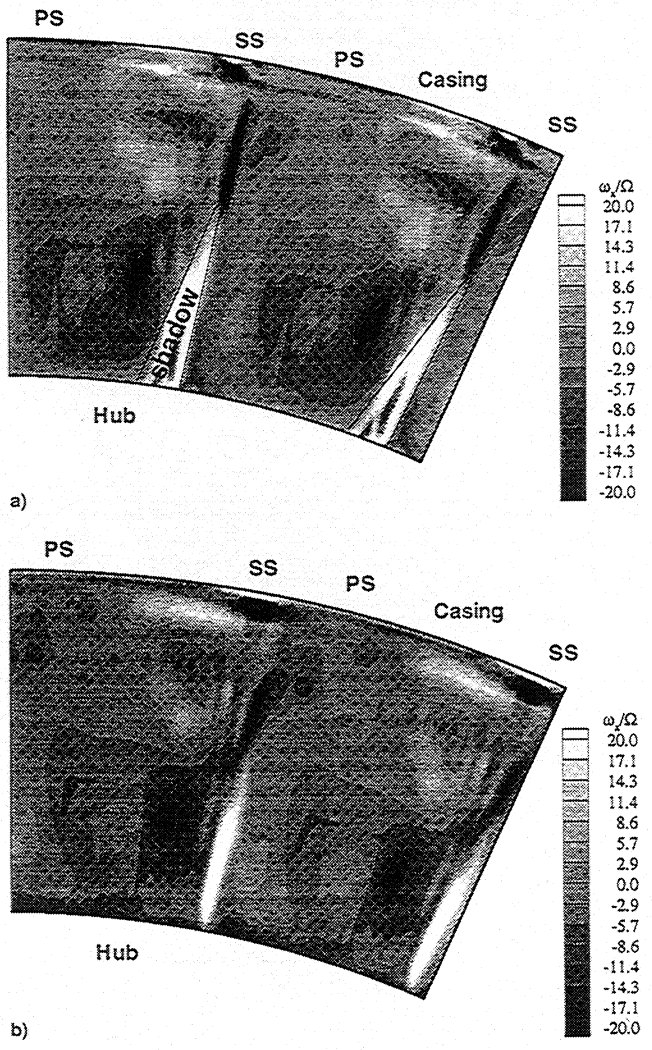

Fig. 11 Axial vorticity ω_x/Ω downstream of the rotor. x/c_r = a) 1.01 and b) 1.10.

Farther downstream at $x/c_r = 1.10$ (Fig. 11), the vorticity structure remains nearly the same as $x/c_r = 1.01$, but at a lower level except in the wake region close to the hub. The positive vorticity region associated with the leakage vortex at the blade suction side-casing corner becomes higher and is expanded at this axial location. The secondary vorticity seems to decay as flow progresses from $x/c_r = 1.01$ to 1.10, but the leakage vorticity and the extent of this increases downstream. The vorticity in the wake-secondary flow interaction region decreases in strength and extent as the flow progresses downstream.

Turbulence Intensity and Stresses

The contours of turbulence intensity components in the intrinsic coordinates (w_s', w_n', and w_r') are shown in Fig. 12. These are normalized by the local total relative velocity. Very high values of turbulence intensities are measured in the tip vortex and secondary flow regions near the casing, and in the wakes. It is interesting to note that the radial components are much higher than the other two components, both in the wake and in the secondary and leakage flow regions. This is a result of the highly anisotropic nature of turbulence. Anisotropy exists not only in the leakage flow and the secondary flow regions, but also in the wake regions, where the turbulence structure is modified by both the rotation and the secondary flow.[12,13] The maximum turbulence intensity in the casing secondary flow region is very high (25%), indicating a highly turbulent nature of flow in the casing-suction surface corner. High-turbulence intensities (15–18%) exist in nearly half of the outer passage.

In the casing half of the passage, there is a high-turbulence level associated with the interaction between the tip leakage flow and the casing secondary flow; it influences most of the outer span. There is also a turbulence structure existing in the leakage-induced separated flow region. Along the top and bottom edges of the negative axial velocity region, where the shear gradients are high (Figs. 8 and 11), the turbulence level is above 25%. The remaining high-turbulence distributions (around 20%) are in the two regions located about 15% pitch from the blade suction side and between $H = 0.75$ and 0.65 and between $H = 0.40$ and 0.30. Through a re-examination of the secondary flows in Fig. 7, it is found that strong variations in the radial velocity occur exactly in these two regions. These two regions are also coincident with the severe wake distortion described in the previous section.

The contour maps of the shear stresses are shown in Fig. 13. The component $\overline{w_n'w_r'}/W^2$ represents the radial component of the turbulent stress and $\overline{w_n'w_s'}/W^2$ is the streamwise component. The highest values of these stresses occur near the casing secondary and leakage flow regions and in the blade wake regions. These are also the regions of large-velocity gradients (Figs. 8 and 9). It is interesting to note that the magnitude of radial and streamwise stresses are of the same order of magnitude. This evidently indicates a nonisotropic nature of turbulence and invalidates the concepts based on isotropic eddy viscosity (constant value in all three directions). In iso-

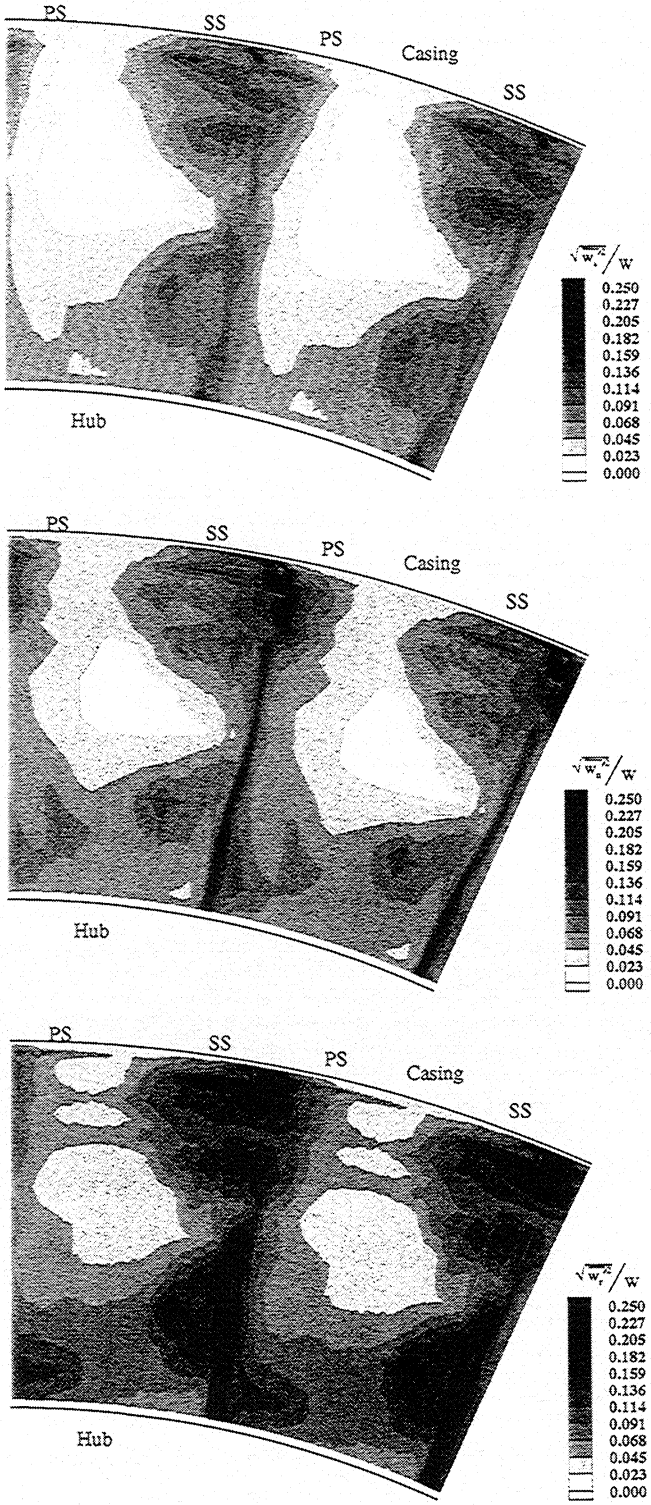

Fig. 12 Contours of measured turbulence intensities in the s, n, and r coordinate system at $x/c_r = 1.10$.

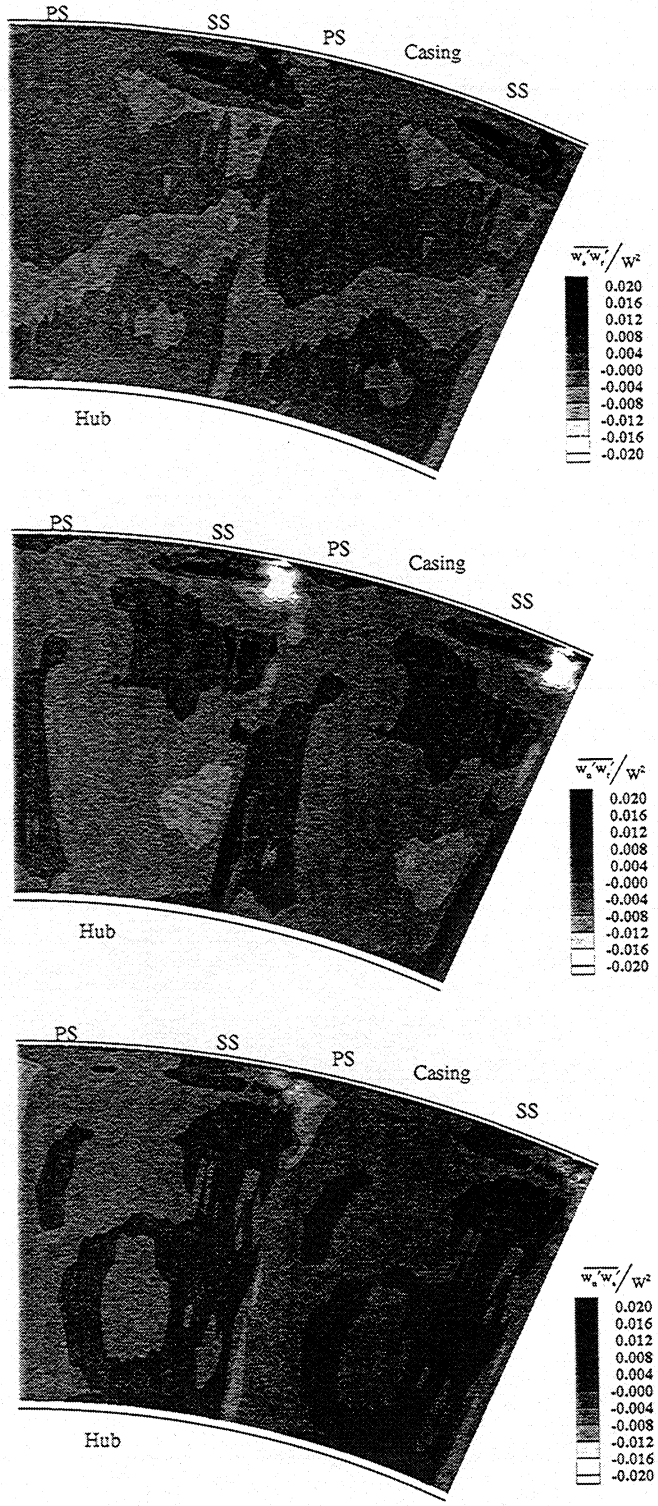

Fig. 13 Shear-stress contours in the s, n, and r coordinate system at $x/c_r = 1.10$.

tropic turbulence models, these stresses are assumed to be in proportion to the local velocity gradient, i.e., $\overline{w_n' w_s'} \sim \mu_t \partial W_s/\partial n$ and $\overline{w_n' w_r'} \sim \mu_t \partial W_r/\partial n$. It is thus clear that the eddy viscosity values in the radial direction should be an order of magnitude higher than that in the streamwise direction, as the measured values of these stress components are nearly equal. It is therefore clear that anisotropic eddy viscosity models, e.g., full Reynolds stress or algebraic Reynolds stress equations, must be used to compute the secondary flow, leakage flow, and wake regions accurately. The anisotrophy results from the complex shear and the curvature effects in the secondary flow and leakage flow regions and the rotation effect in the wake regions.[13] As indicated earlier, the curvature and rotation effects alter the structure of turbulence, with a major influence in the radial direction. Attempts to derive the eddy viscosity values from known stresses and velocity gradients were not successful. The results showed wide scatter and nonphysical values. This further confirms the conclusion that one- and two-equation turbulence models, which utilize the eddy viscosity concept, are not valid in secondary flow, leakage flow, and wake regions.

Rotor Wake Characteristics

The blade wakes play a major role in the rotor/stator interaction, vibration, and noise. The features of the rotor blade wake are examined in this section. The total relative velocity distributions are used for characterization of the rotor wake features and for comparison with the nozzle vane wake analysis performed in the same facility. As demonstrated in the previous section, there are very strong secondary flows and tip leakage flows downstream of the rotor. Their influence on the rotor wake is so powerful that at some radial locations the wake pattern is completely distorted. For these distorted wake patterns, it is found that the velocity defect and the semiwidth cannot be determined unambiguously, and these locations have been omitted from the plots. Near the hub (H = 0.3–0.02), there is an extensive secondary flow region occupying almost the hub-half of the blade passage (Figs. 7 and 11). This secondary flow increases the total relative velocity on the pressure side and decreases it on the suction side, e.g., Fig. 6 at H = 0.10. The secondary flow sweeps the hub endwall flow from the pressure to the suction side, moving the low-momentum fluid to the suction side and high-momentum fluid to the pressure side. The degree of velocity reduction is so severe at H = 0.3 and 0.2 immersions that the wake features (such as velocity defect and semiwidth) are no longer identifiable.

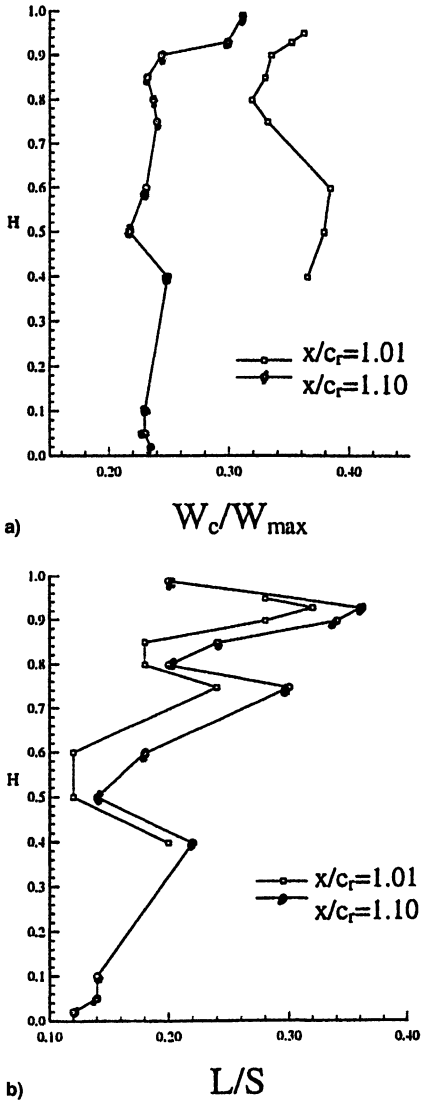

Fig. 14 a) Relative total velocity defect in the wake [defined as $(W_c)/W_{max}$ in the wake]. b) The semiwake width (defined as the width at half the depth of the wake) normalized by the blade pitch.

Similar phenomena are observed for the secondary flow region in the casing-half of the blade passage. For example, the wake pattern at H = 0.70 is so distorted (as distorted as the H = 0.30 radial location shown in Figs. 8 and 9) that no wake features can be identified. Very close to the casing, however, the influence of the tip clearance flow has a dominant effect (H = 0.99–0.93, Figs. 6–9). But, unlike the secondary flows, this influence is confined to the center of the wake; a much smaller influence region than that of the secondary flow.

The velocity defect W_c/W_{max} and the semiwidth (L/S) of the wake are plotted in Fig. 14. The main feature here is the relatively large increase in the velocity defect in the casing region caused by the presence of the strong tip clearance vortex. The wake decay is much more rapid in the midspan region because of the thin, well-defined wake present downstream of the trailing edge of the blade. The wake defect decreases dramatically (by as much as 50%) at the 10% downstream location. In the secondary flow region (H = 0.8), the wakes are not well defined because of the presence of strong passage vortex. The wake defect remains relatively constant at the 10% downstream location over most of the blade passage because most of the radial mixing in the wake has already occurred. As for the semiwidth of the wake, there is an increase in the width radially outward. There are two local peaks at H = 0.75 and 0.4 as a result of the secondary flows, which tend to reduce the total relative velocity on the blade suction side and, thus, to widen the wake. There is an additional peak very close to the casing, which is caused by the tip leakage flow. The secondary flow/wake interaction results in faster decay of the wakes in these regions. The semiwake width at both locations is very similar.

The decay characteristics of the rotor wake velocity defect at midspan is plotted in Fig. 15 along with the decay features of the nozzle wake of the same stage.[8] In addition, some computational results and the experimental data for similar turning (100–110 deg) cascade are also shown.[14] Sitaram and Govardhan's[15] data are from a rotor cascade. The nozzle wake decays faster than the rotor wake. This is most likely caused by the potential interaction (unsteady) between the nozzle and the downstream rotor. The rotor wake decay near the trailing edge (up to 10% of chord in the streamwise direction) is very rapid. Large radial velocities associated with the blade rotation and the associated spanwise mixing in a compressor rotor tend to decay the wakes faster than the stationary blades.[16] But the decay rate slows down downstream of the trailing edge. The decay of the rotor wake is in good agreement with the correlations of Raj and Lakshminarayana.[17]

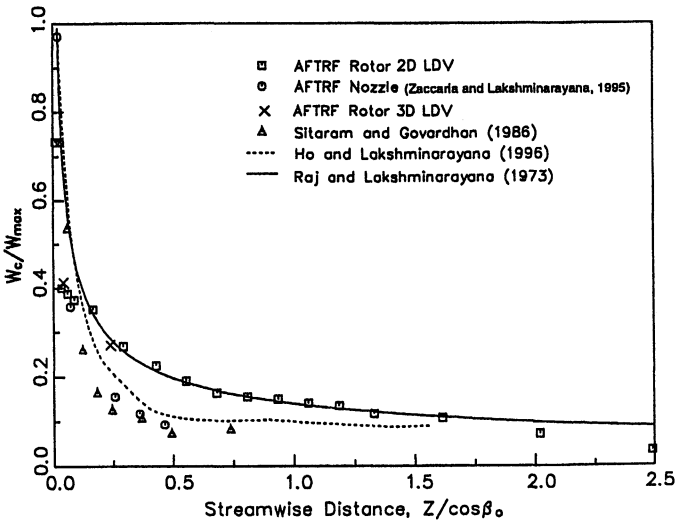

Fig. 15 Wake defect decay downstream of the rotor blade.

Concluding Remarks

The global features of the three-dimensional flowfield downstream of the rotor stage are examined in terms of velocity, vorticity, turbulence, and shear-stress distributions relative to the rotor blade. The hub secondary flow is found to be very strong, well organized, and occupying the entire blade passage. The casing-half secondary flow presents a much more fragmented pattern as a result of the interaction with the leakage flow. The secondary flow–rotor wake interaction region has low radial velocity, high axial vorticity, and high-turbulence intensities (25–30%).

The secondary flow and relative motion between the blade and the casing wall seem to reduce leakage flow, and the leakage vortex is confined to the corner of the suction surface-casing regions. Strong secondary flow, which tends to confine the tip vortex, reduces the diffusion and spreading of the tip vortex downstream. The tip clearance vortex is confined to about 5% of span near the tip. There is a major difference in the behavior of the leakage vortex between those observed in cascades and in the present rotor.

The leakage flow/vortex region is characterized by separated flow, high-turbulence intensity, large underturning, and vorticity. The secondary flow seem to overshadow all other effects from midspan to $H = 0.95$. The overall vorticity field caused by secondary flow (both hub and tip) is much more dominant compared with the leakage vortex, which is confined to a very small region.

The rotor wake pattern is much more disturbed by the three-dimensional flowfield (secondary flows and tip leakage flow) than that observed in the nozzle wake. At some radial locations, the distortion is so severe that the wake features (such as the velocity defect and the semiwidth of the wake) cannot be identified unambiguously. There is an increase in the rotor wake width in the radial direction as a result rotation effects. From hub to midspan, the secondary flow and rotation effects are cumulative in inducing radial outward flow in the wake. From midspan to casing, the secondary flow effects dominate in inducing radial inward velocity in the wake.

The radial turbulence intensity was found to be substantially higher than other components in the secondary and leakage flows and wake regions because of the anisotropy of the turbulent flowfield. Over most of the rotor blade passages, the shear-stress correlation terms are found to be very low, except in the tip vortex and casing passage vortex regions. The maximum absolute values of $\overline{w_n' w_r'}$ are higher than the maximum absolute values of $\overline{w_s' w_r'}$ and $\overline{w_n' w_s'}$, indicating the need to use an anisotropic eddy viscosity model in the computation of the rotor flowfield. In the freestream of the rotor, a substantial increase in the turbulence level (3–8%) was observed compared with the nozzle freestream levels (1.5–2%), and this is caused by the interaction of the nozzle wake and the rotor flowfield.

Acknowledgments

This work was sponsored by NASA Lewis Research Center, NAG3 1736 (R. Boyle and C. Civinskas were the Technical Monitors) and by the U.S. Army Research Office, DAAH04-95-1-0179 (T. Doligalski was the Technical Monitor). The assistance of H. Petrie and J. Posada Garcia is gratefully acknowledged.

References

[1]Langston, L. S., Nice, M. L., and Hooper, R. M., "Three-Dimensional Flow Within a Turbine Blade Passage," *Journal of Engineering for Power*, Vol. 99, No. 1, 1977, pp. 21–28.

[2]Sieverding, S. H., "Recent Progress in the Understanding of Basic Aspects of Secondary Flows in Turbine Blade Passages," *Journal of Engineering for Gas Turbine and Power*, Vol. 107, No. 2, 1985, pp. 248–257.

[3]Gregory-Smith, D. G., Walsh, J. A., Graves, C. P., and Fulton, K. P., "Turbulence Measurements and Secondary Flows in a Turbine Rotor Cascade," *Journal of Turbomachinery*, Vol. 110, 1988, pp. 479–485.

[4]Yamamoto, A., "Endwall Flow/Loss Mechanisms in a Linear Turbine Cascade with Blade Tip Clearance," *Journal of Turbomachinery*, Vol. 111, No. 3, 1989, pp. 264–275.

[5]Joslyn, D., and Dring, R., "Three-Dimensional Flow in an Axial Turbine: Part 1—Aerodynamic Mechanisms," *Journal of Turbomachinery*, Vol. 114, No. 1, 1992, pp. 61–70.

[6]Gallus, H. E., Zeschky, J., and Hah, C., "Endwall and Unsteady Flow Phenomena in an Axial Turbine Stage," *Journal of Turbomachinery*, Vol. 117, No. 4, 1995, pp. 562–570.

[7]Lakshminarayana, B., Camci, C., Halliwell, I., and Zaccaria, M., "Design, Development and Performance of Turbine Facility," *International Journal of Turbo and Jet Engines*, Vol. 13, No. 3, 1996, pp. 155–172 (AIAA Paper 92-3325, 1992).

[8]Zaccaria, M., and Lakshminarayana, B., "Investigation of Three-Dimensional Flowfield at the Exit of a Turbine Nozzle," *Journal of Propulsion and Power*, Vol. 11, No. 1, 1995, pp. 55–63.

[9]Suder, K. L., Hathaway, M. D., Okiishi, T. H., Strazisar, A. J., and Adamczyk, J. J., "Measurements of the Unsteady Flow Fields Within the Stator Row of a Transonic Axial Flow Fan, Part I: Measurements and Analysis Technique," American Society of Mechanical Engineers, ASME Gas Turbine Conference and Exhibit, Paper 87-GT-226, American Society of Mechanical Engineers, New York, 1987.

[10]Suryavamshi, N., Lakshminarayana, B., and Prato, J., "Unsteady Total Pressure Field Downstream of an Embedded Stator in a Multistage Axial Flow Compressor," *Journal of Fluids Engineering*, Vol. 119, No. 4, 1997, pp. 985–994.

[11]Ristic, D., Lakshminarayana, B., and Chu, S., "Three-Dimensional Flow Field at the Exit of an Axial Flow Turbine," NASA CR 206601, 1998.

[12]Anand, A. K., and Lakshminarayana, B., "An Experimental Study of the Three-Dimensional Boundary Layers and Turbulence Characteristics Inside a Rotating Channel," *Journal of Engineering for Power*, Vol. 100, No. 4, 1978, pp. 76–090.

[13]Lakshminarayana, B., and Reynolds, B., "Turbulence Characteristics in the Near Wake of a Compressor Rotor Blade," *AIAA Journal*, Vol. 18, No. 11, 1980, pp. 1354–1362.

[14]Ho, Y., and Lakshminarayana, B., "Computational Modeling of Three-Dimensional Flow Through a Turbine Rotor Cascade with Strong Secondary Flows," *Journal of Turbomachinery*, Vol. 118, No. 2, 1996, pp. 250–261.

[15]Sitaram, N., and Govardhan, M., "Effect of Incidence Angle on Wake Characteristics of a High Deflection Turbine Rotor Linear Cascade," 9th Australasian Fluid Mechanics Conf., Australasian Fluid Mechanics Committee, 1986.

[16]Ravindranath, A., and Lakshminarayana, B., "Mean Velocity and Decay Characteristics of the Near and Far Wake of a Compressor Rotor Blade of Moderate Loading," *Journal of Engineering for Power*, Vol. 102, No. 4, 1982, pp. 535–548.

[17]Raj, R., and Lakshminarayana, B., "Characteristics of the Wake Behind a Cascade of Aerofoils," *Journal of Fluid Mechanics*, Vol. 61, Pt. 4, 1973, pp. 707–730.